

# Two perspectives on amplified warming over tropical land

Suqin Duan<sup>1</sup>, Suqin Q. Duan<sup>2</sup>, Karen A. McKinnon<sup>2,3</sup>, and Isla R. Simpson<sup>4</sup>

<sup>1</sup>Affiliation not available

<sup>2</sup>Institute of the Environment and Sustainability, University of California

<sup>3</sup>Departments of Statistics and Data Science, and Atmospheric and Oceanic Sciences, University of California

<sup>4</sup>Climate and Global Dynamics Laboratory, National Center for Atmospheric Research

December 28, 2023



10 ABSTRACT: Climate change projections show amplified warming associated with dry conditions  
11 over tropical land. We compare two perspectives explaining this amplified warming: one based on  
12 tropical atmospheric dynamics, and the other focusing on soil moisture and surface fluxes. We first  
13 compare the full spatiotemporal distribution of changes in key variables in the two perspectives  
14 under a quadrupling of CO<sub>2</sub> using daily output from the CMIP6 simulations. Both perspectives  
15 center around the partitioning of the total energy/energy flux into the temperature and humidity  
16 components. We examine the contribution of this temperature/humidity partitioning in the base  
17 climate and its change under warming to rising temperatures by deriving a diagnostic linearized  
18 perturbation model that relates the magnitude of warming to (1) changes in the total energy/energy  
19 flux, (2) the base-climate temperature/humidity partitioning, and (3) changes in the partitioning  
20 under warming. Using CMIP6 output, we show that the spatiotemporal structure of warming is  
21 well predicted by the inverse of the base-climate partition factor, which we term the base-climate  
22 sensitivity: conditions that are drier in the base climate have a higher base-climate sensitivity  
23 and experience more warming. On top of this relationship, changes in the partition factor under  
24 intermediate (between wet and dry) surface conditions further enhance or dampen the warming.  
25 We discuss the mechanistic link between the two perspectives by illustrating the strong relationships  
26 between lower tropospheric temperature lapse rates, a key variable for the atmospheric perspective,  
27 and surfaces fluxes, a key component of the land surface perspective.

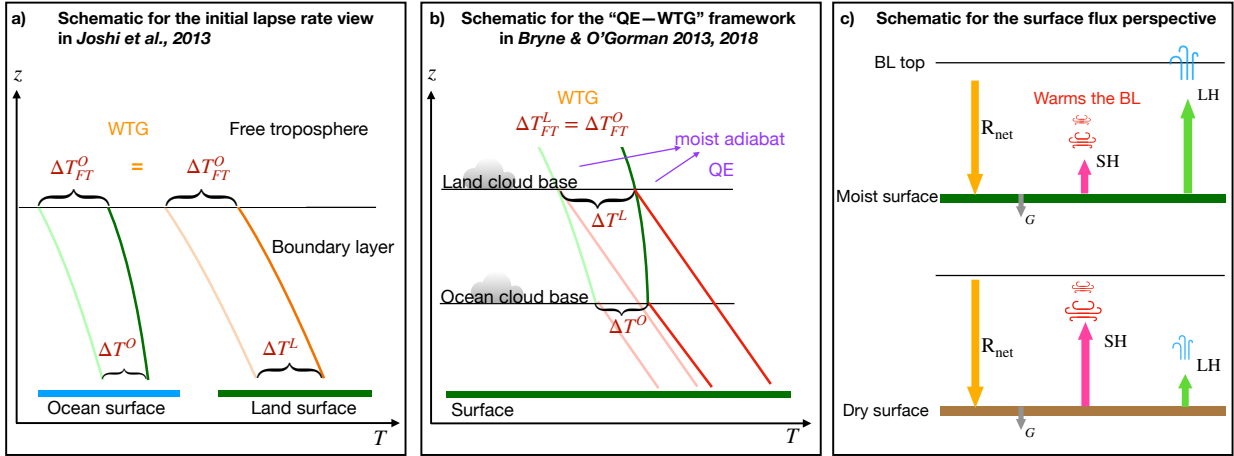
28 SIGNIFICANCE STATEMENT: Understanding what conditions give rise to the largest magni-  
29 tude of warming in response to rising CO<sub>2</sub> concentrations is not only scientifically important but  
30 also critical from a climate impacts standpoint. Two main perspectives, one focusing on atmo-  
31 spheric dynamics and the other focusing on land surface processes, have been proposed to explain  
32 the stronger warming associated with drier conditions in the tropics. Here, we compare and contrast  
33 these two perspectives. Using climate model output, we demonstrate that amplified warming can  
34 largely be predicted from base-climate dryness alone in both perspectives, but is further modified  
35 based on changes in the partitioning of energy between temperature and moisture. We highlight the  
36 spatiotemporal conditions where assumptions in the two perspectives hold and where deviations  
37 occur.

## 38 **1. Introduction**

39 The manner in which temperatures are expected to change regionally with global warming is  
40 not only an important scientific question, but also a critical issues for climate change impacts and  
41 adaptation. Previous studies using climate models have shown that land warms more than the  
42 ocean (e.g., Sutton et al. 2007; Joshi et al. 2008, 2013; Byrne and O’Gorman 2013, 2018) and,  
43 over tropical land, days at high temperature percentiles warm more than the average, resulting in  
44 an elongated upper tail and exacerbated hot extremes (e.g., Duan et al. 2020; Byrne 2021). This  
45 “amplified” warming over land seems to be associated with drier conditions: land is drier than the  
46 ocean, and those days at the high percentiles of the temperature distribution are days with dry soils  
47 and low relative humidity.

51 Two main perspectives have been proposed to explain this drier-warmer relationship. One  
52 perspective is based on tropical atmospheric dynamics (Joshi et al. 2013; Byrne and O’Gorman  
53 2013, 2018). Weak temperature gradients in the tropical upper troposphere (WTG; Sobel and  
54 Bretherton 2000) lead to approximately spatially-uniform temperatures. Below, the uniform free  
55 tropospheric temperatures are connected to the surface by a temperature lapse rate closer to a moist  
56 adiabat over a moist surface such as the ocean and closer to a dry adiabat over a drier surface  
57 such as the land. The larger lapse rate over the drier surface corresponds to higher surface air  
58 temperature. Upon warming, the moist adiabatic lapse rate reduces, while the dry adiabatic lapse  
59 rate does not change; this, combined with the lack of temperature gradients in the free troposphere,

60 enhances the base-climate temperature gradient across land and ocean and leads to a land-ocean warming contrast (Joshi et al. 2013, the schematics are reproduced in Fig. 1a).



48 FIG. 1. (a, b) Schematics of cited studies that explain the amplified warming over land with the atmospheric  
 49 dynamics perspective. In (a) and (b), lines with faint colors show temperature profiles in the base climate; and  
 50 lines with bright colors show temperature profiles in the warm climate.

61  
 62 Building upon this argument, Byrne and O’Gorman (2013) made the arguments of Joshi et al.  
 63 (2013) more quantitative by using the concept of quasi-equilibrium (QE; Arakawa and Schubert  
 64 1974; Emanuel et al. 1994; Neelin and Zeng 2000). QE together with WTG suggests that the  
 65 temperature profile in the free tropical troposphere approximately follows the moist adiabat with  
 66 minimal horizontal gradients. Below the cloud base in the boundary layer, the temperature profile  
 67 follows a dry adiabat (schematics shown in Fig. 1b). The higher the cloud base, the longer path in  
 68 the lower troposphere where temperature follows the dry adiabat, the warmer the surface.

69 With the theoretical bases of QE and WTG, this framework (the “QE–WTG” framework here-  
 70 after) can be expressed into mathematical forms by making two assumptions: (1) an atmospheric  
 71 dynamics constraint that the increase of the boundary layer moist static energy (MSE) across land  
 72 and ocean is uniform, and (2) a moisture constraint that the change of  $q$  over land is a fraction ( $\gamma$ ) of  
 73 that over ocean. This fraction  $\gamma$  comes from the base-climate ratio of  $q$  over land to  $q$  over ocean,  
 74 and is assumed to remain constant with climate change. Because the base-climate humidity ratio  
 75  $\gamma$  is on average less than 1, land moistens less and warms more than the ocean. This “QE–WTG”  
 76 framework was initially applied to explain the mean warming contrast over land and ocean (Byrne

77 and O’Gorman 2013, 2018), and has since been adjusted to explain the amplified warming of the  
78 hot tail of the temperature distribution over tropical land (Byrne 2021).

79 In contrast to the atmospheric dynamics based perspective is a land surface based perspective.  
80 The surface perspective instead emphasizes changes in the partitioning between sensible and  
81 latent heat fluxes in response to moisture availability and/or changes in plants’ physiology (e.g.,  
82 Seneviratne et al. 2010; Berg et al. 2014; Donat et al. 2017; Vogel et al. 2017; Duan et al. 2020;  
83 Dirmeyer et al. 2021). When sufficient water is available for evapotranspiration, a greater portion of  
84 the net radiation at the surface ( $R_n$ ) is released as latent heat (LH), which does not directly increase  
85 the surface air temperature (schematic in Fig. 1c). When the soil gets sufficiently dry and/or plants’  
86 stomata close, the ratio of  $R_n$  that can be released through LH reduces. Consequently, the surface  
87 warms more and sensible heat (SH) fluxes increases, which warms the near-surface air. In this  
88 surface perspective, soil moisture, or the Bowen ratio (the ratio of SH to LH) critically controls the  
89 warming magnitude.

90 Although both perspectives involve a partition of the total energy between moistening and  
91 warming, there is a gap between the perspectives. The atmospheric perspective is used primarily  
92 by the atmospheric dynamics community, and its reasoning relies on constraints that are end  
93 products of atmospheric variables in an equilibrium state without explicit links to the changes in  
94 soil moisture or vegetation dynamics that the surface perspective emphasizes. In fact, the moisture  
95 constraint in the QE-WTG framework is derived from an “ocean influence model” (Chadwick  
96 et al. 2016; Byrne and O’Gorman 2016, 2018). The surface perspective is familiar to the land-  
97 atmosphere interaction community, and is process-based, but the physical constraints are based  
98 on the local surface energy balance and there is a lack of connection to atmospheric processes  
99 and to the global constraints offered by the atmospheric dynamics perspective. Furthermore, the  
100 atmospheric perspective has mainly been invoked to explain large-scale (e.g. averaged across  
101 zonal bands and/or over land and ocean) and time-mean changes (only recently applied to daily  
102 time scales; Byrne 2021); whereas the surface perspective has widely been used for local extreme  
103 days (e.g., Donat et al. 2017; Vogel et al. 2017; Duan et al. 2020; Dirmeyer et al. 2021).

104 In addition, there is a nuanced question regarding whether the climatological dryness, or the  
105 change in dryness in response to increased CO<sub>2</sub>, is more important for amplified warming (dryness  
106 is measured by specific humidity in the atmospheric perspective and soil moisture in the surface

107 perspective). In the QE–WTG framework, the moisture constraint parameter  $\gamma$  is calculated based  
108 on the base-climate specific humidity alone, i.e., the amplified warming can be predicted for regions  
109 that are climatologically dry (base-climate  $\gamma$  smaller than one), whereas the surface perspective  
110 often emphasizes *changes* in the soil moisture or surface flux partition with climate change. This  
111 difference can cause confusion especially when the decrease of relative humidity (RH) or the  
112 increase of climate aridity (measured by P/PET in the cited work) are discussed together with the  
113 amplified warming (Sherwood and Fu 2014; Fu and Feng 2014; Byrne and O’Gorman 2018): one  
114 may wonder whether more drying leads to more warming, or more warming leads to more drying.

115 In order to understand the equivalency, or lack thereof, between the two perspectives, we examine  
116 the following questions in the context of climate models:

- 117 (1) Do the key variables in the two perspectives correspond to each other?
- 118 (2) How do the dryness measures between the two perspectives relate to each other?
- 119 (3) How do climatological dryness versus changes in dryness contribute to amplified warming  
120 in each perspective?

121 Motivated by these questions, we first compare the full spatiotemporal distribution of key vari-  
122 ables and their changes in the two perspectives using a process-based phase space of daily soil  
123 moisture and the climatological aridity index, which captures both the temporal variability and the  
124 climatological spatial variations in dryness (Duan et al. 2023). In the phase space, we can visualize  
125 how each perspective manifests both across climatologically dry and wet regions as measured by  
126 the climatological aridity index (AI), and across temporal variability in dryness and wetness within  
127 locations that have similar AIs. The data and frameworks we use are introduced in Section 2. We  
128 discuss the applicability of the QE-WTG framework to explaining the spatiotemporal distribution  
129 of warming and examine the moisture constraint’s connection with the land surface in Section 3.  
130 We then use a diagnostic linearized perturbation model (see also Zeppetello et al. 2020; Chan  
131 et al. 2022, for applications in land-atmosphere interactions) to discuss the relative roles of the  
132 base-climate dryness versus the change in dryness for the magnitude of warming in Section 4.  
133 This linearized perturbation model also offers an alternative way to view the connection of the two  
134 perspectives. We briefly comment on the mechanistic connection of the two perspectives via the  
135 association of the lower tropospheric temperature lapse rate to surface flux partition in Section 5  
136 and provide a final summary in Section 6.

## 137 2. Data and Methods

### 138 *Data*

139 We analyze simulations submitted to the Coupled Model Intercomparison Project  
140 Phase 6 (CMIP6; Eyring et al. 2016). We take the first 30 years (1850–1879) in the histori-  
141 cal experiment as the control (base) climate state, and years 121–150 in the abrupt-4×CO<sub>2</sub> (4×CO<sub>2</sub>  
142 for short) experiment as the perturbed climate state. Climate changes in variables are charac-  
143 terized by subtracting the base state from the perturbed climate state. We use the outputs from  
144 nine models that have reported daily values of near-surface (2 m) air temperature ( $T$ ), specific  
145 humidity ( $q$ ), relative humidity (RH), surface soil moisture (SM, moisture in the top 10 cm soil  
146 layer), surface latent heat flux (LH), surface sensible heat flux (SH), and upwelling and down-  
147 welling shortwave and longwave radiative fluxes from which we calculate the net radiation at  
148 the surface ( $R_n$ , downward positive), for both the historical and 4×CO<sub>2</sub> experiments. The nine  
149 models are: CanESM5, CMCC-ESM2, GFDL-CM4, MIROC6, IPSL-CM6A-LR, INM-CM5-0,  
150 MPI-ESM-1-2-HAM, MPI-ESM1-2-HR, and MRI-ESM2-0. The limitation to these specific nine  
151 models mainly comes from the availability of surface soil moisture and surface flux outputs at  
152 daily frequency in the 4×CO<sub>2</sub> experiment (e.g., daily SM is not available for CESM2, and daily  
153 surface and radiative fluxes are not available for the ACCESS and EC-Earth models). Besides the  
154 limitation due to the data availability, we only include one model from each modeling institution  
155 even if outputs from the different versions of that model are available. In this case, we consider the  
156 more recent version, or the higher resolution version that has the more complete set of variables  
157 available. NorESM2-MM, FGOALS-g3, TaiESM1 have also reported daily surface soil moisture,  
158 but a large amount of the soil moisture values are invalid and therefore they are not included.  
159 In addition to the variables listed above, precipitation  $P$  in the historical experiment is used in  
160 order to calculate the climatological Aridity Index (AI). AI is defined as  $AI = 0.8R_n/(L_vP)$ . Arid  
161 regions have larger AI under this definition, and the constant 0.8 is set empirically to account for  
162 the fact that not all available energy goes into evapotranspiration even if soil moisture is abundant  
163 (Milly and Dunne 2016; Koster and Mahanama 2012). To calculate the near surface air moist static  
164 energy (MSE,  $MSE = c_pT + L_vq + gz$ , where  $c_p$  is the specific heat of dry air,  $T$  is the surface air  
165 temperature,  $L_v$  is the latent heat of vaporization,  $q$  is the surface air specific humidity,  $g$  is the

166 gravitational acceleration, and  $z$  is the height above sea level), we also use the orographic height  
167 variable. Since the orographic height will not change with climate change, we only need this  $gz$   
168 term when calculating MSE in one climate state. Temperature and geopotential height on pressure  
169 levels (variable  $ta$  and  $zg$ ) during 1850–1879 in the historical experiment are used to calculate  
170 the temperature lapse rate between 700 hPa and the surface. Since MRI-ESM2-0 only reports  
171 daily 3D variable after 1950, and daily 3D  $zg$  from CMCC-ESM2 is not available, we use only  
172 the remaining seven models for temperature lapse rates and profiles. We use the grid-cell land  
173 area fraction variable to select land grid cells as those with a land area fraction  $\geq 99\%$ . Since  
174 we are interested in situations where we expect a strong land surface control on temperature, we  
175 focus on the warm season, which we define as the 150 days centered on July 15 for the Northern  
176 Hemisphere, and the 150 days centered on Jan 15 for the Southern Hemisphere.

### 177 *The daily soil moisture/climatological aridity index (SM/AI) phase space*

178 The land surface is highly heterogeneous: it ranges from very arid regions such as the Sahara  
179 desert to very moist regions such as the Amazon forest. For a given location, temporal variability  
180 of dryness/wetness can substantially affect the surface latent heat flux: LH that is more than  
181  $150 \text{ W/m}^2$  during average days can reduce to only a few tens of  $\text{W/m}^2$  when the soil is dry (see  
182 Fig. A1g). Furthermore, when considering changes of these hydroclimatic variables under climate  
183 change, more complexity comes into play due to the non-linear relationship between LH and soil  
184 moisture. In particular, for a fixed amount of net radiation at the surface, LH increases with SM  
185 in the transitional regime but is not sensitive to SM in the dry and wet regimes (e.g., Seneviratne  
186 et al. 2010) and decreases with SM in the active-rain regime (Duan et al. 2023). As a result,  
187 when soil dries under climate change, LH decreases in the transitional regime while increases in  
188 the wet regime due to increases in net radiation (Duan et al. 2023). These different changes in  
189 LH can lead to different responses in surface air temperature: warming will be magnified in the  
190 transitional regime due to reductions in latent cooling, in contrast to the behavior in the wet regime.  
191 Since places with different climatological dryness have different percentages of days in each of  
192 the LH–SM regimes, averaging over time that contains both local wet and dry days, or averaging  
193 over locations with different local soil moisture distributions can lead to substantial canceling of  
194 signals and result in an averaged behavior that is hard to interpret. Moreover, models represent

195 the spatiotemporal distribution of soil moisture and the evapotranspiration–soil moisture functions  
196 differently, resulting in further uncertainty.

197 Duan et al. (2023) presented a process-based phase space constructed using daily soil moisture  
198 and the climatological aridity index and showed that, when organizing the highly heterogeneous  
199 land hydroclimatic variables in this phase space, one can acquire coherent patterns of changes across  
200 models and across variables. The coherent patterns in this SM/AI phase space are in contrast to  
201 the highly uncertain results in the geographical map view (Fig. S3 of Duan et al. (2023)). Here  
202 we adopt this method, and process the model fields that have dimensions of calendar days and  
203 geographical locations into phase-space grids consisting of 50 temporal bins and 50 spatial bins.  
204 The horizontal axis of the phase space is formed by the temporal bins, and calculated by sorting  
205 the original data according to the daily SM and placing 2% of the 4500 days in each bin. These  
206 temporal bins represent local dry days to wet days. The vertical axis of the phase space is formed by  
207 the spatial bins, and calculated by sorting the original grid cells (for both the base and the 4×CO<sub>2</sub>  
208 climate states) according to the *base-climate* warm-season mean AI and placing 2% of the tropical  
209 land area (30°S–30°N) in each bin. These spatial bins represent the climatologically moist regions  
210 to climatologically arid regions. We then take the area-weighted average of data in each bin and  
211 plot the bin-average values as shadings. Fig. A1 and Fig. 3 show a number of variables and their  
212 changes displayed in this SM/AI phase space. We refer to the average in each of the 50×50 bins as  
213 data “under a certain spatial-temporal condition”. We normalize changes in variables in the phase  
214 space by the tropical mean ocean warming  $[\overline{T}]_o$  in each model before averaging over models to  
215 accounts for the different climate sensitivities across models.

### 216 *The diagnostic linearized model for the magnitude of warming*

217 Both perspectives consider a partitioning of a total energy (MSE) or energy flux ( $R_n$ ) between a  
218 temperature component ( $c_p T$  or SH) and a humidity component ( $L_v q$  or LH). Here we reduce the  
219 variables in the balance relations and rearrange them to relate the temperature component to the  
220 total energy/energy flux by a partition factor. When considering climate change, we decompose  
221 changes in the total energy/energy flux into a component with an unchanged base-state partition  
222 factor and a component representing the contribution from changes in this partition factor. This  
223 method of decomposition helps us compare the partitioning in the two perspectives, and diagnose

224 the relative importance of the base-climate dryness versus the change in dryness under climate  
 225 change in contributing to the amplified warming over tropical land. Distinguishing between the  
 226 role of the base climate state and changes to that state is important, because information about the  
 227 base climate state is also available from observations, and can be used to make predictions and  
 228 constrain climate change projections. We derive the relations below.

229 In the surface flux perspective, the total net energy flux received by the surface is the net radiation  
 230  $R_n$ .  $R_n$  is largely balanced through the surface sensible heat flux (SH) and the surface latent heat  
 231 flux (LH), with a small component  $G$  going into the ground. In general, the surface energy  
 232 balance  $R_n - G = \text{SH} + \text{LH}$ , can be approximated as  $R_n \approx \text{SH} + \text{LH}$ . The Bowen ratio,  $B = \text{SH}/\text{LH}$ ,  
 233 summarizes the relative partitioning between SH and LH. When the Bowen ratio is higher, more of  
 234 the incoming heat goes into SH, which warms the near-surface air. Using  $B$ , we can write  $\text{SH} + \text{LH}$   
 235 as  $(B + 1)B^{-1}\text{SH}$ , and then have

$$R_n \approx \text{SH} + \text{LH} = \frac{B + 1}{B} \text{SH} = \Psi \text{SH} \quad (1)$$

236 where  $\Psi = (B + 1)/B \approx R_n/\text{SH}$ . In this way, we associate the total energy flux to SH through a  
 237 ratio  $\Psi$ . Below, we link SH to temperature. The inverse,  $1/\Psi$ , is the fraction of  $R_n$  balanced by  
 238 SH, and is strongly related to the dryness of the surface (i.e., soil moisture).

239 While the surface flux perspective is based on partitioning of the net radiative flux, the atmo-  
 240 spheric dynamics perspective is based on partitioning of the total energy MSE, which is assumed  
 241 to be uniform across the tropics in QE-WTG theory. Leaving aside the  $gz$  term in MSE that will not  
 242 change under warming, the moist enthalpy ( $\text{ME} = c_p T + L_v q$ ) consists of a temperature component  
 243  $c_p T$  (the dry specific enthalpy), and a moisture component  $L_v q$ . By a similar approach to that used  
 244 above for surface fluxes, we can use the ratio between these two components as  $b = (c_p T)/(L_v q)$   
 245 to write ME as

$$\text{ME} = \text{MSE} - gz = c_p T + L_v q = \frac{b + 1}{b} c_p T = \psi c_p T, \quad (2)$$

246 where  $\psi = (b + 1)/b = \text{ME}/(c_p T)$ . In this way, we associate the total energy to surface air  
 247 temperature, through a ratio  $\psi$ . The inverse,  $1/\psi$ , is the fractional contribution of the temperature  
 248 component in the total ME. Thus, the surface energy and atmospheric dynamic views can be

249 written in somewhat comparable forms (see Table 1), and we will compare these parameters and  
 250 their changes in the remainder of the paper.

251 Under climate change, the variables in Eqs. 1 and 2 can be expressed as a base state combined  
 252 with a perturbation ( $\Delta$ ). By dropping the non-linear interaction terms between the perturbations  
 253 (residuals of the linearization are shown in Fig. B1ab in Appendix B), the equations that govern  
 254 the atmospheric and land perspectives can be written as,

$$\Delta\text{MSE} = \Delta\text{ME} \approx \psi c_p \Delta T + c_p T \Delta\psi, \quad (3)$$

255 and

$$\Delta R_n \approx \Psi \Delta\text{SH} + \text{SH} \Delta\Psi \quad (4)$$

$$\approx \Psi \kappa \Delta T + \text{SH} \Delta\Psi \quad (5)$$

256 In Eq. 5, we have assumed that  $\Delta\text{SH} = \kappa \Delta T$  where  $\kappa$  is a constant i.e., the sensible heat flux  
 257 anomalies can be linearly related to the temperature anomalies using a proportionality constant,  
 258 following the concepts in Vargas Zeppetello and Battisti (2020); Chan et al. (2022); Kong et al.  
 259 (2023). This allows the land perspective to be written in terms of a dependence on  $\Delta T$ , analogous to  
 260 the atmosphere perspective. We examine this assumption in more detail and discuss its limitations  
 261 in Appendix C. It is important to note that MSE is an energy that directly contains the  $T$  component,  
 262 while  $R_n$  is a flux balanced by two fluxes that affect and are affected by  $T$  and  $q$ . This leads to a  
 263 more exact relationship between  $\Delta T$  and  $\Delta\text{ME}$  in Eq. (3) while a more approximate relationship  
 264 that relies on an additional parameter,  $\kappa$ , in Eq. (5).

265 From here, we can write the temperature change in association with either a change in MSE or  
 266  $R_n$  as:

$$\Delta T = \frac{\Delta\text{MSE} - c_p T \Delta\psi}{c_p \psi}, \quad (6)$$

267 and

$$\Delta T = \frac{\Delta R_n - \text{SH} \Delta\Psi}{\kappa \Psi}. \quad (7)$$

268 In Eq. 6 and Eq. 7,  $\Delta\text{MSE}$  and  $\Delta R_n$ —change of the total energy or energy flux—can be regarded  
 269 as analogs of the “forcing” used in studies of climate sensitivity and feedbacks (Roe 2009; Held

270 and Shell 2012; Zelinka et al. 2020). Because we analyze the changes between two climate  
271 states approximately in equilibrium, the “forcing” terms include changes in climate that lead to  
272 equilibration, such as increases in upwelling longwave radiation. Therefore, they are a combination  
273 of forcing and response, but we can understand these responses of the total energy and energy flux  
274 as relatively externally constrained (external to the temperature response), and we analyze the  
275 temperature response given these changes in the total energy/energy flux (the forcing analog).

276 The terms  $(c_p\psi)^{-1}$  in Eq. 6 and  $(\kappa\Psi)^{-1}$  in Eq. 7 can be understood as the sensitivity of the  
277 temperature response to the forcing analog (the total energy/energy flux). The specific heat of dry  
278 air,  $c_p$ , is a physical constant. For simplicity, we also consider  $\kappa$  to be a constant as discussed above.  
279 Therefore, in the following sections, we take  $\psi^{-1}$  and  $\Psi^{-1}$  as the sensitivities in each framework,  
280 which are solely determined by the base-climate state.

281 The terms  $-c_pT\Delta\psi$  and  $-\text{SH}\Delta\Psi$  are the contribution of the change in the partition factor ( $\psi$   
282 and  $\Psi$ , the inverse of which is the sensitivity discussed above) to the magnitude of warming, and  
283 we refer to them as the “repartition” terms. Specifically, the terms summarize the *changes* in  
284 the partitioning of MSE into  $T$  and  $q$  for the atmospheric framework, or the partitioning of  $R_n$   
285 into SH and LH for the surface energy balance framework. The sign of the repartition terms is  
286 consistent with their effect on the temperature response: positive values indicate that the balance  
287 is repartitioning in a way that will increase the temperature response, and decrease the moisture  
288 response.

289 A summary of the balance relations, their linearized perturbation equations and relevant terms  
290 for the two perspectives are listed in Table 1.

### 293 **3. Comparing the two perspectives across the spatiotemporal distribution**

294 Previous results based on the QE-WTG framework (Byrne and O’Gorman 2013, 2018; Byrne  
295 2021) are often displayed in terms of zonal averages, and results from the surface perspectives  
296 (e.g., Donat et al. 2017; Vogel et al. 2017) are often reported as a temporal maxima (or the highest  
297 percentiles). Here we compare the full spatiotemporal distribution of key variables in the two  
298 perspectives. To do so, we employ the SM/AI phase space as described in Section 2. Recall that in  
299 this phase space, the horizontal axis captures temporal variability as measured by local daily soil  
300 moisture (SM) percentiles, and the vertical axis captures spatial variability as measured by the

291 TABLE 1. A summary of the equations and terms considered for the base-climate physics and climate change  
 292 perturbations in the atmospheric-dynamics and the surface-flux perspectives.

Constraint	Balance	Partition factor	Derived relation
MSE (ME)	$ME = MSE - gz = c_p T + L_v q$	$b = \frac{c_p T}{L_v q}, \psi = \frac{b+1}{b}$	$ME = \psi c_p T$
$R_n$ ( $R$ )	$R = R_n - G = SH + LH$	$B = \frac{SH}{LH}, \Psi = \frac{B+1}{B}$	$R = \Psi SH$

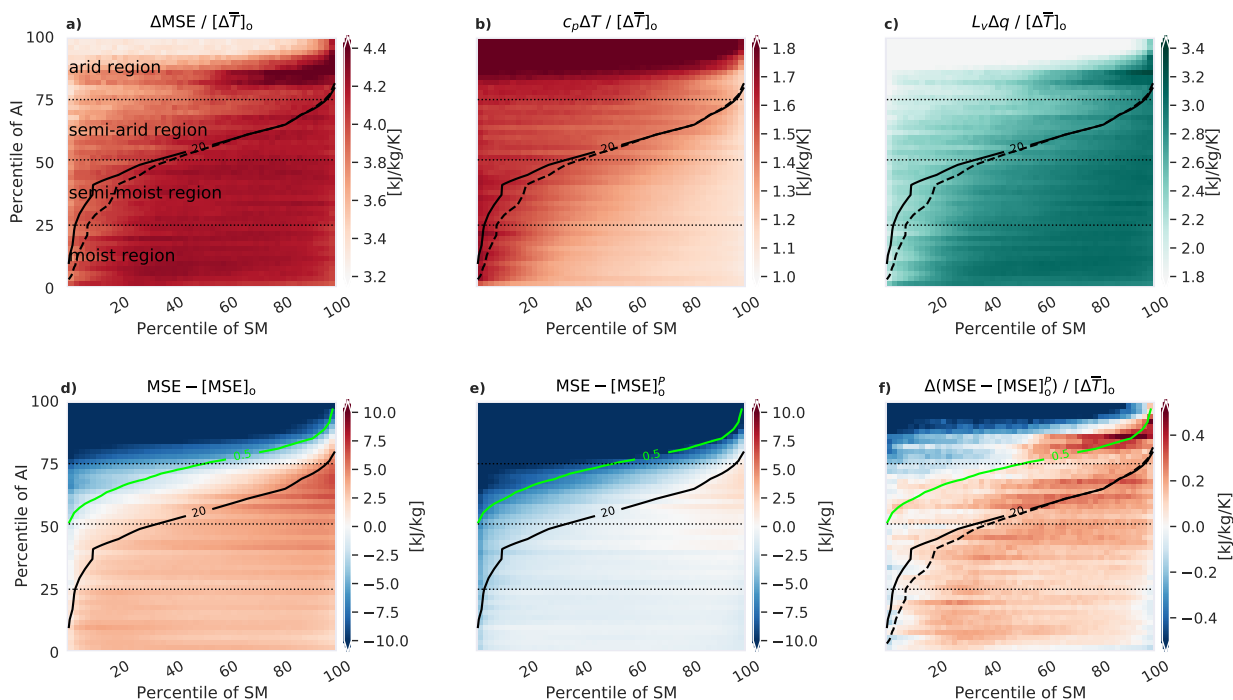
Linearized perturbation relation	$T$ response	Sensitivity	Change of the total	Repartition term
$\Delta MSE \approx \psi c_p \Delta T + c_p T \Delta \psi$	$\Delta T \approx \frac{\Delta MSE - c_p T \Delta \psi}{c_p \psi}$	$\frac{1}{c_p \psi}$	$\Delta MSE$	$-c_p T \Delta \psi$
$\Delta R_n \approx \Psi \kappa \Delta T + SH \Delta \Psi$	$\Delta T \approx \frac{\Delta R_n - SH \Delta \Psi}{\kappa \Psi}$	$\frac{1}{\kappa \Psi}$	$\Delta R_n$	$-SH \Delta \Psi$

301 climatological Aridity Index (AI) percentiles. The isoline of a surface soil moisture value of 20  
 302  $\text{kg/m}^2$  is shown as a black contour (solid for the base climate and dashed for the  $4 \times \text{CO}_2$  climate).  
 303 This line roughly indicates the critical soil moisture,  $\text{SM}_{\text{crit}}$ , that marks the transitional regime in  
 304 the Budyko curve where soil moisture limits evapotranspiration and the soil moisture-temperature  
 305 feedback is the strongest. While its specific value can vary across models, time, and region, this  
 306 value can be used as a rough indicator in CMIP6 models (Duan et al. 2023). To the lower-right  
 307 of this line are wetter conditions, both spatially and temporally, and to the upper-left are drier  
 308 conditions.

### 309 *a. The atmospheric perspective*

322 In the atmospheric perspective, change of the total energy ( $\Delta \text{MSE}$ , Fig. 2a) is split, by definition,  
 323 between warming ( $c_p \Delta T$ , Fig. 2b) and moistening ( $L_v \Delta q$ , Fig. 2c).  $\Delta \text{MSE}$  (Fig. 2a) shows an  
 324 increase across all  $50 \times 50$  temporal and spatial bins with a value ranging from 3.3 to more than  
 325 4.2 kJ/kg per degree of mean tropical ocean warming. The warming magnitude ( $\Delta T$ , Fig. 2b) is  
 326 smaller in moist conditions (lower right) while it is larger in dry conditions (upper left), maximizing  
 327 over the desert regions. Warming around the critical soil moisture contours in moist regions is  
 328 also strong, and this amplified warming center around  $\text{SM}_{\text{crit}}$  is more evident in changes of the

## The atmospheric perspective



310 FIG. 2. Changes in the surface air (a) moist static energy (MSE), (b) temperature converted to energy units  
 311 ( $c_p T$ ), (c) specific humidity converted to energy units ( $L_v q$ ), between the  $4 \times \text{CO}_2$  climate state and the base  
 312 climate state displayed in the phase space of daily soil moisture percentiles (horizontal axis), and climatological  
 313 Aridity Index percentiles (vertical axis). (d) Deviation of the moist static energy (MSE) over land from the  
 314 corresponding (corresponding day and latitude) zonal mean values over the ocean ( $[\text{MSE}]_o$ ) in the base climate;  
 315 (e) deviation of the MSE over land from the corresponding precipitation-weighted zonal mean values over the  
 316 ocean ( $[\text{MSE}]_o^P$ ) in the base climate, (f) changes of the deviation of the land MSE from  $[\text{MSE}]_o^P$  between the  
 317  $4 \times \text{CO}_2$  climate state and the base climate state. Changes of variables are normalized by the mean tropical ocean  
 318 warming  $[\Delta \bar{T}]_o$  in each model before averaging over the models. The black contours (solid for the base climate  
 319 and dashed for the  $4 \times \text{CO}_2$  climate) are the isolines of the surface soil moisture value of  $20 \text{ kg/m}^2$  which roughly  
 320 marks the conditions in the transitional regime of the Budyko curve. The green contour is the isline of the daily  
 321 mean precipitation rate of  $0.5 \text{ mm/day}$ . See text for more details.

329 daily-maximum temperature (not shown). Specific humidity  $q$  increases under all conditions, and  
 330 the magnitude is generally contrary to that of  $\Delta T$ , i.e., wetter conditions moisten more and warm  
 331 less, while drier conditions moisten less and warm more.

332 Mathematically, the QE–WTG framework (Byrne and O’Gorman 2013, 2018; Byrne 2021)  
 333 predicts warming over land as:

$$\begin{aligned}\Delta T^L &= (\Delta \text{MSE}^L - L_v \Delta q^L) / c_p = (\Delta \text{MSE}^O - \gamma L_v \Delta q^O) / c_p \\ &= \Delta T^O + (1 - \gamma) \frac{L_v}{c_p} \Delta q^O\end{aligned}\quad (8)$$

334 In this equation, the super-script  $L$  and  $O$  denote land and ocean, as in the original work.  $\gamma$ , as  
 335 mentioned in the Introduction, is the ratio of  $q^L$  to its corresponding zonal mean value over the  
 336 ocean in the base climate ( $\gamma = q^L / q^O$ ).  $\gamma$  is assumed to be constant with climate change and  
 337 therefore  $\Delta q^L = \gamma \Delta q^O$ .

338 In the QE–WTG framework,  $\Delta \text{MSE}$  is generally assumed to be uniform across various divisions  
 339 of the tropics. For example, Byrne and O’Gorman (2013, 2018) assumed uniform annual-mean  
 340 changes across land and ocean for a given latitude, and Byrne (2021) showed uniform changes in  
 341 CMIP6 models for the upper 50 MSE percentiles across time and locations over land and ocean.  
 342 With this assumption, amplified warming is then predicted in conditions with less moistening. The  
 343 general “less moistening–more warming” correspondence we see in Fig. 2b and Fig. 2c seem to be  
 344 consistent with the theory of this QE-WTG framework. However, it is interesting to note that we  
 345 also see the less moistening-more warming relationship over the desert, despite the fact that there  
 346 is almost no moist convection over the desert, so the region is not expected to be in convective  
 347 quasi-equilibrium as required by the theory. Indeed, as we can see in Fig. 2a, the change in MSE is  
 348 noticeably smaller in deserts than other regions, since there is a lack of coupling between the desert  
 349 boundary layer and other regions that are dominated by moist convection. Thus, the assumption of  
 350 equal change in MSE that has been applied previously to other groupings of regions in the tropics  
 351 appears to break down in the phase space we consider, particularly in the drier days and regions  
 352 that warm the most.

353 To further test the QE–WTG framework regarding the assumption about the uniform MSE in the  
 354 AI/SM phase space, we compare the MSE at a certain spatiotemporal condition over land to the  
 355 corresponding day and latitude zonal mean values over ocean in the base climate in Fig. 2d. If all  
 356 conditions satisfy QE and WTG (especially QE, since WTG holds relatively well across locations in  
 357 the tropics, see Fig. 6c), the values in Fig. 2d should be approximately zero, indicating that MSE over

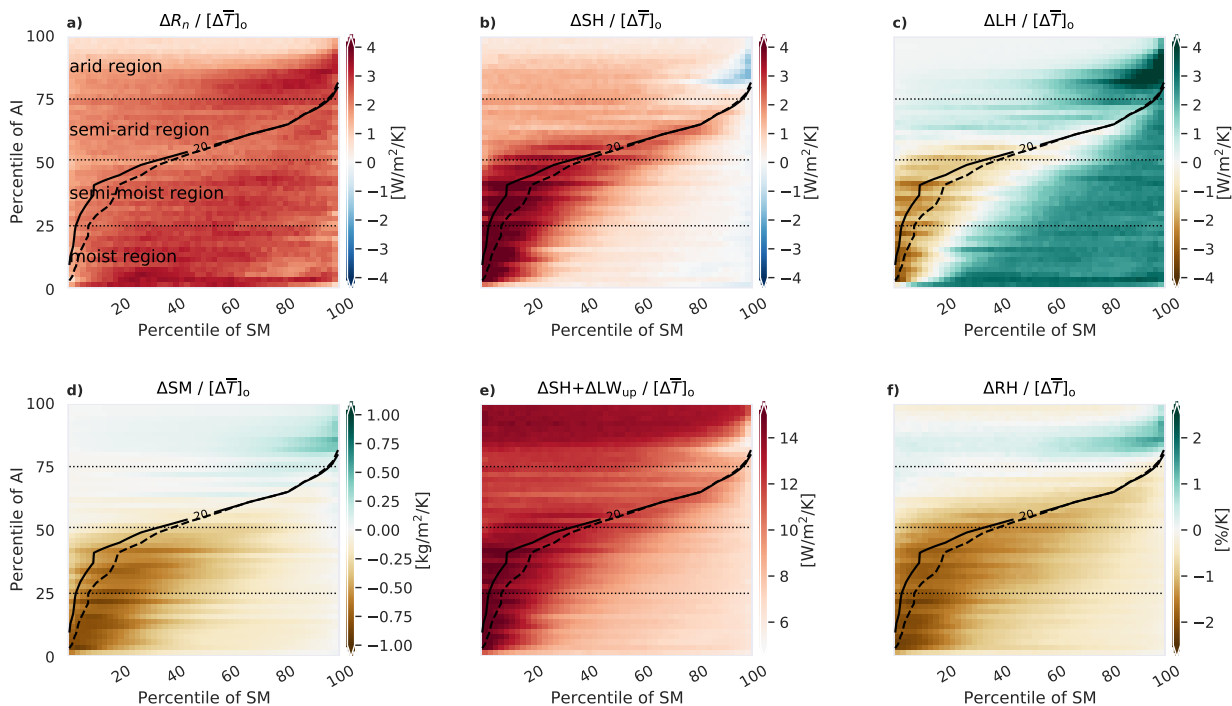
358 land roughly equals the corresponding value over the ocean. However, Fig. 2d shows greater-than-  
 359 zero values for wet conditions and less-than-zero values for dry conditions. Zhang and Fueglistaler  
 360 (2020) showed that this equal-MSE assumption holds better when conditioned on precipitating  
 361 situations (we refer to this as the revised equal-MSE assumption below). Following their approach,  
 362 Fig. 2e shows the MSE at each location over land with the corresponding *precipitation-weighted*  
 363 zonal mean values over ocean ( $[\text{MSE}]_o^P$ ) subtracted. We can see that most of the moist conditions  
 364 (to the right of the black line of the  $\text{SM}_{\text{crit}}$ , or the green isoline of the precipitation rate 0.5 mm/day)  
 365 approximately satisfy the revised equal-MSE assumption. For dry conditions, land MSE still  
 366 deviates from  $[\text{MSE}]_o^P$  by more than 10 kJ/kg. This deviation is expected because, as mentioned  
 367 above, these very dry conditions do not satisfy the QE assumption that relies on active moist  
 368 convection.

369 QE-WTG suggests equal MSE over land and ocean in each of the base and the warm climate  
 370 states, from which the equal *change* of MSE over land and ocean is derived. Fig. 2f shows changes  
 371 of the MSE deviation from the precipitation-weighted ocean zonal mean value over land between  
 372 the warm and the base climate states, i.e.,  $\Delta(\text{MSE} - [\text{MSE}]_o^P)$ . Note that even in the moist conditions  
 373 where the difference between land and ocean is close to 0 in the base climate (to the lower right  
 374 of the black line in Fig. 2e), the MSE increase over land with climate change is still larger than  
 375 the increase over the precipitating ocean. The magnitude of this deviation (difference between  
 376 MSE increases over land and ocean) can be as large as 0.3–0.5 kJ/kg (0.3–0.5 K in temperature  
 377 units) for each degree of tropical mean ocean warming. Thus, while these assumptions are  
 378 necessary to form the over-arching theory of QE–WTG, and have been used to successfully explain  
 379 the behavior of climatological averages over large domains (e.g. land and ocean averages), their  
 380 accuracy diminishes when considering the spatiotemporal distribution in this manner. In applying  
 381 the QE-WTG framework to extreme temperature at the daily time scale, Byrne (2021) added a term  
 382 ( $\Delta h$ ) to address the smaller changes in MSE during hot days over land that are evident in our phase  
 383 space (Fig. 2f).

### 384 *b. The surface perspective*

393 For the surface flux perspective, changes in the total energy flux, i.e., the net radiation at the  
 394 surface ( $R_n$ ; Fig. 3a) are partitioned between changes in the surface sensible heat flux ( $\Delta\text{SH}$ , Fig. 3b)

### The surface perspective



385 FIG. 3. Changes in the surface air (a) surface net radiation ( $R_n$ ), (b) surface sensible heat flux (SH), (c) surface  
 386 latent heat flux (LH), and (d) soil moisture (SM), (e) SH plus upwelling longwave radiation ( $SH + LW_{up}$ ), and (f)  
 387 relative humidity (RH) between the  $4 \times CO_2$  climate state and the base climate state, displayed in the phase space  
 388 of daily soil moisture percentiles (horizontal axis), and climatological Aridity Index percentiles (vertical axis).  
 389 Changes in these variables are normalized by the mean tropical ocean warming  $[\Delta \bar{T}]_o$  in each model before  
 390 averaging over the models. The black contours (solid for the base climate and dashed for the  $4 \times CO_2$  climate) are  
 391 the isolines of the surface soil moisture value of  $20 \text{ kg/m}^2$  which roughly marks the conditions in the transitional  
 392 regime. See text for more details.

395 and changes in the surface latent heat flux ( $\Delta LH$ , Fig. 3c), with a negligible change in ground heat  
 396 fluxes (not shown).  $R_n$  increases under all spatiotemporal conditions of dryness and wetness,  
 397 with the maximum increase in wet conditions (around  $3 \text{ W/m}^2$  per degree of ocean warming) and  
 398 smallest increase over the desert (around  $1 \text{ W/m}^2$  per degree of ocean warming). The pattern  
 399 of  $\Delta R_n$  across the spatiotemporal states is highly similar to the pattern of  $\Delta MSE$  (Fig. 2a); their  
 400 correlation across the 2500 bins in the phase space is 0.85. This close correspondence between  
 401 the changes in the total energy in the surface air and changes in the total energy flux at the surface

402 may be explained by the following two possibilities: one is that increases in  $R_n$  drive the increases  
403 in MSE; the other is that increases in  $q$  (Fig. 2c), which is the dominant component in  $\Delta$ MSE  
404 (Fig. 2a), result in increases in  $R_n$  through the increased radiative emissivity of moister air.

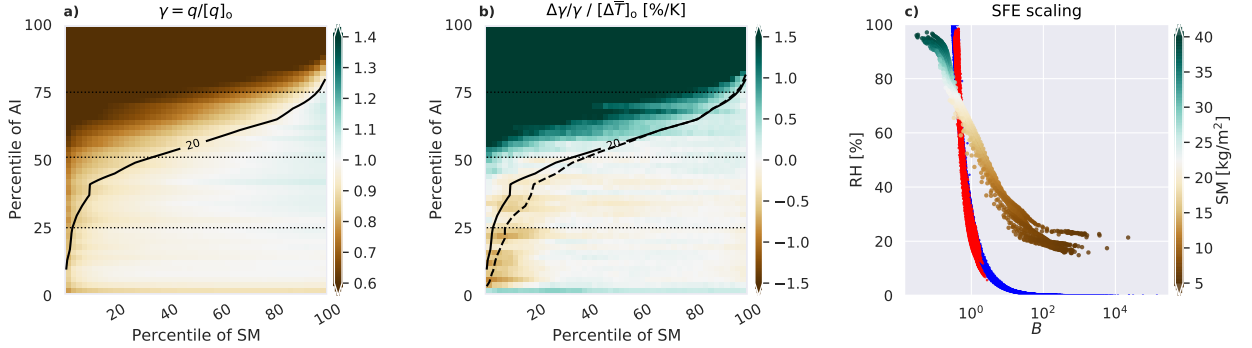
405 Except for the very dry conditions where changes in LH are near-zero, and the transitional  
406 conditions around  $SM_{crit}$  where LH decreases and SH increases, changes in  $R_n$  are predominantly  
407 balanced by increases in LH. In particular, in the wet conditions (those to the right of  $SM_{crit}$ ), LH  
408 increases by about 2–3 W/m<sup>2</sup> per degree of mean ocean warming, while SH changes much less  
409 (or even decreases), by  $\pm 1$  W/m<sup>2</sup> per degree of mean ocean warming. Recall that, in these same  
410 moist locations and times, increases in specific humidity also dominate the increases in MSE, and  
411 the warming magnitude is similar to that over ocean (Fig. 2b).

412 For the transitional conditions around  $SM_{crit}$ , decreases in LH are substantial (Fig. 3c). The  
413 decrease in LH is driven by drying of SM (Fig. 3d, also indicated by shift of the  $SM_{crit}$  isoline to  
414 higher percentiles), and is compensated by strong increases in SH. The increase in SH and decrease  
415 in LH in the transitional conditions correspond to amplified warming in these conditions (Fig. 2b),  
416 reflecting the role of surface flux repartitioning in exacerbating the warming. It is interesting to  
417 note, however, that even though LH decreases in these transitional conditions, specific humidity  
418 increases (Fig. 2c). This reflects the role of other sources and sinks of surface air specific humidity  
419 besides the local land surface evapotranspiration. Meanwhile, RH decreases (Fig. 3f), suggesting  
420 that specific humidity has not increased enough to match the increase in the saturation specific  
421 humidity. RH is often taken as a reflection of the atmospheric dryness; the decrease of RH  
422 along  $SM_{crit}$  despite the increase of the specific humidity indicates that soil moisture–temperature  
423 feedback is an important contributor to the decrease of RH over land.

424 In arid regions (upper quarter of the phase space), in the base climate state, LH is small (deserts  
425 are dry) and  $R_n$  is predominantly balanced by SH. With climate change, changes in LH will be  
426 small (deserts remain deserts) and we might expect large increases in SH, corresponding to the  
427 pronounced warming (Fig. 2a). However, we see here that changes in SH in these arid regions are  
428 also small. This is because both the surface and near surface air warm substantially, and the increase  
429 of long wave radiation (which scales with  $T^4$ ) is faster than the increase of SH (which scales with  
430  $T$ ); i.e., upwelling long wave radiation ( $LW_{up}$ ) is partly playing the role in the energy balance that  
431 is played by SH in other regions. Adding changes in  $LW_{up}$ , Fig. 3e reproduces the pronounced

432 increases in the arid regions. Nevertheless, increases in  $R_n$  in these arid regions are small and the  
 433 surface energy balance ( $R_n \approx SH + LH$ ) is still obeyed. The comparisons in Fig. 3abce here are  
 434 consistent with and supplement the discussion of surface flux changes under different regimes of  
 435 the temperature distribution change in Duan et al. (2020).

436 *c. A discussion on the moisture constraint*



437 FIG. 4. (a) the land–ocean specific humidity ratio (the  $\gamma$  in Byrne and O’Gorman (2013, 2018), calculated as  
 438 the specific humidity  $q$  at each land grid cell divided by the corresponding ocean zonal mean specific humidity  
 439  $[q]_o$ ), (b) fractional changes in  $\gamma$  normalized by  $[\Delta\bar{T}]_o$ , displayed in the phase space of daily soil moisture  
 440 percentiles (horizontal axis), and climatological Aridity Index percentiles (vertical axis). The black contour is  
 441 the isoline of the surface soil moisture value of  $20 \text{ kg/m}^2$ . (c) RH and the Bowen ratio  $B$ . Each dot represents  
 442 one bin among the  $50 \times 50$  spatial-temporal bins in the AI/SM phase space as in Fig. 3 and 5, and is color-coded  
 443 by its SM value in the base climate. The blue/red dots in panel (c) show the theoretical scaling by the Surface  
 444 Flux Equilibrium, red using RH to calculate  $B$  and blue using  $B$  to calculate RH. See text for more details.

445 As mentioned in Sections 1 and 3a, the stronger warming predicted over land in the QE–WTG  
 446 framework emerges from the moisture constraint that  $\Delta q^L = \gamma \Delta q^O$ , which is derived based on  
 447 the transport of atmospheric moisture from the ocean (Byrne and O’Gorman 2016; Chadwick  
 448 et al. 2016). While the derivation of this moisture constraint emphasizes ocean control – specific  
 449 humidity over land is assumed to follow specific humidity over ocean, which increases with  
 450 warming approximately at the rate of the Clausius-Claperton scaling – land specific humidity is  
 451 also affected by land-atmosphere exchanges (e.g. Van der Ent et al. 2010). A drier land surface  
 452 will tend to result in lower evapotranspiration and, for a given amount of moisture convergence  
 453 (although the two do not operate independently), a smaller  $\gamma$ . When the moisture constraint is

454 applied to climate model simulations, the value of  $\gamma$  is calculated as the local climatological  $q^L$   
 455 at each land grid cell divided by the corresponding zonal mean  $q^O$  (Byrne and O’Gorman 2016,  
 456 2018), and is spatially-variable. Therefore, the moisture constraint (atmospheric perspective)  
 457 contains information of the spatially-variable surface dryness (surface perspective). Note that the  
 458 results in Byrne and O’Gorman (2016, 2018) were presented as averages over latitudinal bands or  
 459 the entire 40°S–40°N domain, which is an average across the underlying variability of  $\gamma$ .

460 We use the same method as in Byrne and O’Gorman (2016, 2018) to calculate  $\gamma$  on each day,  
 461 and present its spatiotemporal distribution in the SM/AI phase space in Fig. 4a. Examining across  
 462 the spatiotemporal distribution,  $\gamma$  ranges from less than 0.2 in the very arid regions to about 1.2 in  
 463 the wettest days (high local SM percentiles) in semi-arid and semi-moist regions. The lowest row  
 464 (the lowest AI percentile bin) contains many grid cells in the upwind slope of the Tibetan Plateau  
 465 where it rains heavily from the orographic lifting; therefore AI is small ( $AI \propto R_n/P$ ) but the specific  
 466 humidity (and  $\gamma$ ) is not necessarily high (since temperature is low at high orographic altitude).

467 Under climate change, the moisture constraint assumes that the ratio  $\gamma$  remains constant, but  
 468 this may not hold if evapotranspiration changes are substantial and not compensated by changes in  
 469 moisture convergence. The change in  $\gamma$  is shown in Fig. 4b. We first draw the readers’ eye to the  
 470 decrease of  $\gamma$  aligning along the critical soil moisture lines where changes in surface conditions  
 471 are the strongest as emphasized by the surface perspective (see Section 3b). In Fig. 4b, for each  
 472 degree warming,  $\gamma$  decreases by about 1% in the water-limited transitional regime for the CMIP6  
 473 multi-model mean. This suggests that, when  $q^O$  increases by 7%/K,  $q^L$  in these conditions, due  
 474 to the decrease of  $\gamma$ , will increase by 6%/K (taking the log and then taking the climate change  
 475 difference on both sides of  $q^L = \gamma q^O$  yields  $\Delta q^L/q^L = \Delta q^O/q^O + \Delta\gamma/\gamma$ ). For  $q^L \approx 16$  g/kg  
 476 ( $L_v q^L \approx 40$  kJ/kg, see Fig. A1c), the 1% change in  $\gamma$  will produce a deviation of about 0.4 kJ/kg  
 477 in  $L_v \Delta q^L$  (which, assuming an accurate constraint of  $\Delta$ MSE by QE and WTG, leads to a 0.4 K  
 478 deviation in the prediction of  $\Delta T^L$ ), for each degree of ocean mean warming. In applying the  
 479 QE-WTG framework to predict the magnitude of land warming, this deviation brought by the  
 480 moisture constraint assumption will partly compensate the deviation brought by the equal MSE  
 481 assumption (the MSE increase in these conditions is smaller, see Fig. 2a and f). Note that in these  
 482 transitional conditions where  $\gamma$  decreases, LH also decreases (Fig. 3c). While we do not perform  
 483 a moisture budget analysis here, this correspondence suggests the role of changing land-sourced

484 moisture in controlling changes in  $\gamma$ . In Byrne (2021) which applies the QE-WTG framework to  
 485 discuss warming of the upper temperature percentiles, both the drier base-climate  $q$  and a decrease  
 486 of RH on those high temperature percentile days contribute to the amplified warming, and both of  
 487 these have connections to the land surface.

488 Another domain in the phase space in Fig. 4b that shows perceptible changes in  $\gamma$  is over the  
 489 arid land regions:  $\gamma$  increases by a much larger fractional rate. The driving mechanism for this  
 490 increase is not yet clear: at the top soil moisture percentiles in these arid regions, both rainfall and  
 491 LH (see Fig. 3c) increase; the overall increase in  $\gamma$  and the moistening at the top soil moisture  
 492 percentiles in these arid regions can result from both changes in the transport of moisture and local  
 493 evapotranspiration.

494 While the atmospheric community conceptually emphasize the ocean control on  $\gamma$  as discussed  
 495 above, the land community emphasizes the land control. In particular, the theory of “Surface Flux  
 496 Equilibrium” (SFE) from the land community (McColl et al. 2019; McColl and Rigden 2020)  
 497 derived that

$$\text{RH} = \frac{c_p}{L_v \phi} \frac{1}{B} \quad (9)$$

498 where  $\phi$  is the derivative of saturation specific humidity  $q^*(T)$  with respect to temperature ( $\phi =$   
 499  $\frac{\partial q^*}{\partial T}|_{T_{BL}} = \frac{L_v q^*}{R_v T_{BL}^2}$ ). This SFE is derived with the assumption that the boundary-layer RH is in  
 500 equilibrium at and beyond daily timescales and the surface heating from SH balances surface  
 501 moistening from LH (i.e., other sources and sinks for the BL heat and moisture budgets are  
 502 neglected). The implication of SFE (Eq. 9) is that, if we know the Bowen ratio, we can know the  
 503 boundary layer RH, and vice versa.

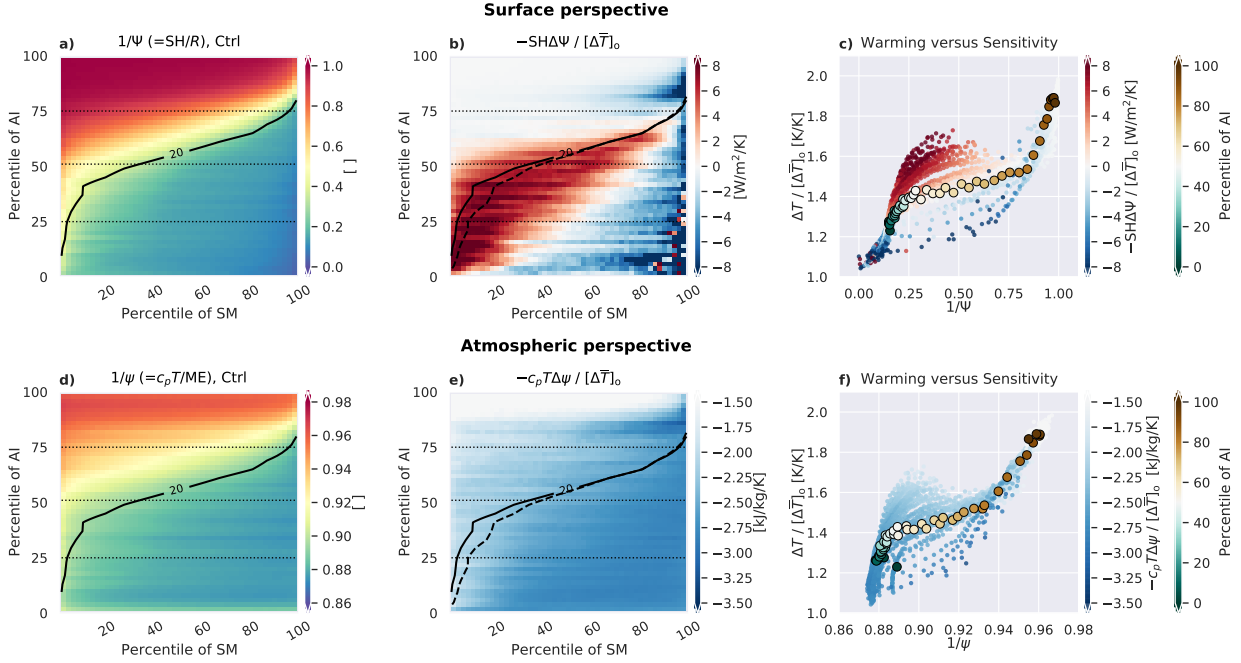
504 Boundary layer RH in the base climate can be effectively regarded as an key indicator for the  
 505 warming/moistening partition in the atmospheric perspective, similar to  $\gamma$ : while  $\gamma$  is the key  
 506 parameter in the mathematical form of the QE–WTG framework, the physical intuition for the  
 507 importance of base climate moisture in controlling warming magnitude draws upon the cloud-base  
 508 height above which the temperature lapse rate shifts to follow a moist adiabat from a dry adiabat  
 509 (see Fig. 1b). The cloud-base height is tightly related to the boundary-layer RH (Betts 2009),  
 510 and therefore the base climate state of both can be regarded as the key control for the warming  
 511 magnitude under the atmospheric perspective. In fact, when Byrne and O’Gorman (2013) first  
 512 formed the QE-WTG framework based on equal equivalent potential temperature  $\theta_e$  over land and

513 ocean, the decomposition for the land/ocean warming ratio was based on RH. Altogether, the SFE  
514 relation in Eq. 9 that directly associates RH with the Bowen ratio, is directly relating the key control  
515 in the atmospheric perspective to the key control in the surface perspective.

516 Fig. 4c shows the relationship between RH and the Bowen ratio  $B$  for each box in the SM/AI  
517 phase space, with the color indicating the soil moisture. RH shows an inverse relationship with  
518  $B$ , as expected. This inverse relationship suggest a strong land surface origin for the boundary  
519 layer RH: the surface influences RH through both controlling the source of water vapor through  
520 evapotranspiration and affecting temperature. The red and blue dots in Fig. 4c show the results  
521 when assuming SFE (Eq. 9; red dots use RH to calculate  $B$  and blue dots use  $B$  to calculate  
522 RH). SFE qualitatively captures the inverse relationship between RH and  $B$ , but there are notable  
523 deviations from what is simulated by the climate models, which likely result from the assumptions  
524 made in the derivations of SFE, although uncertainties of model parameterization of surface fluxes  
525 may have also contributed. For example, in wet conditions (green dots in Fig. 4c), SFE-based RH  
526 is higher than the actual RH, since moisture would likely be transported out of the boundary layer.  
527 In dry conditions (brown dots in Fig. 4c) SFE-based RH is lower than the actual RH because water  
528 vapor can be transported into dry regions. Contributions from these non-surface processes would  
529 moderate the atmospheric RH for a given Bowen ratio. While some of these correspondences may  
530 seem intuitive, we make them explicit because soil moisture and its changes do not appear directly  
531 in the QE-WTG framework, while studies based on the surface flux perspective do not typically  
532 rely on the behavior of the large-scale transport of moisture.

#### 533 **4. Base-climate sensitivity and changes in partition in the two perspectives**

541 To what extent can the two perspectives explain the spatiotemporal warming pattern over land  
542 in climate models? Recall that in Section 2, we derived a relationship between the magnitude of  
543 warming in each perspective and three components: changes of the total energy/energy flux, the  
544 base-climate partition between the temperature and the moisture component (the inverse of which  
545 is termed the base-climate sensitivity), and the changes in this base-climate partition (Eqns. (6),  
546 (7)). The comparison of various relations for the two perspectives is listed in Table 1. In the  
547 following we examine the spatiotemporal distribution of the base-climate partition and its changes  
548 under warming, and the contribution of the base-state partition versus its changes to the warming



534 FIG. 5. (a, d) the base-climate sensitivity ( $1/\Psi$  and  $1/\psi$ ), (b, e) the repartition term ( $-SH\Delta\Psi$  and  $-c_pT\Delta\psi$ ;  
 535 a positive sign corresponds to a repartition towards enhancing warming), and (c, f) the relationship between  
 536 the magnitude of warming  $\Delta T$  (normalized by mean tropical ocean warming  $[\Delta T]_o$ ) and the base climate  
 537 sensitivity in the surface (c) and the atmospheric (f) perspectives. Small dots in (c) and (f) represent the  $50 \times 50$   
 538 spatiotemporal bins, and are color-coded by the repartition terms as shown in (b) and (e); large dots in (c) and (f)  
 539 are the temporally-averaged values of warming and base-climate sensitivity for the 50 spatial bins, color-coded  
 540 by percentiles of the aridity index (AI).

549 magnitude. This alternative way of decomposition provides us a complementary view of the two  
 550 perspectives.

551 Figures 5a and d show the spatiotemporal distribution of the base-climate sensitivity. For  
 552 both the surface (Fig. 5a) and the atmospheric (Fig. 5d) perspectives, the base-climate sensitivity  
 553 is larger for drier conditions (upper-left) and smaller for wetter conditions (lower-right). Recall  
 554 that in the surface perspective, base-climate sensitivity  $\Psi^{-1} = SH/R \approx SH/R_n$  is the ratio of  
 555 the surface sensible heat flux to the total net radiation; and in the atmospheric perspective, base-  
 556 climate sensitivity  $\psi^{-1} = c_pT/ME$  is the ratio of the temperature component of energy (dry specific  
 557 enthalpy) to the total moist enthalpy. Both reflect the dryness in the base climate, because they  
 558 indicate how much of the available energy/energy flux is partitioned into temperature/heating rather

559 than moisture/evapotranspiration. The correlation between the atmospheric and surface sensitivity  
560 is high (0.99, see also Fig. 6a), reflecting the tight connection of the two perspectives in the base  
561 climate.

562 The surface sensitivity  $1/\Psi$  (Fig. 5a) ranges from 0 to 1: values over the desert are close to  
563 1, indicating that  $R_n$  at the surface is almost entirely balanced by SH; values in very high SM  
564 percentiles over moist and semi-moist regions are close to 0, indicating that  $R_n$  is almost entirely  
565 balanced by LH. The atmospheric sensitivity  $1/\psi$  (Fig. 5d), however, has a smaller range and is  
566 generally higher than the surface sensitivity (ranges from 0.88 for moist regions to 0.96 for arid  
567 regions). This indicates that in one climate state, for a given location, the near surface dry specific  
568 enthalpy ( $c_p T$  around 300 kJ/kg, see Fig. A1b in Appendix A) dominates the total moist static  
569 energy (around 325 in arid regions to 345 kJ/kg in moist regions, see Fig. A1a). This is in contrast  
570 to the *variability* across the spatiotemporal distribution, and the *climate change* values, for which  
571 the latent energy ( $L_v q$ ) values dominate those in surface air MSE.

572 Fig. 5b and e show the repartition term in Eq. 6 and Eq. 7. The repartition term captures the  
573 contribution of changes in the partition factor ( $\psi$  and  $\Psi$ ) to warming. The patterns of the repartition  
574 terms  $-c_p T \Delta\psi$  and  $-SH \Delta\Psi$  are dominated by the patterns of changes in the partition factor  $-\Delta\Psi$   
575 and  $-\Delta\psi$  (compare Fig. 5be with Fig. B1dc in Appendix B). In the surface perspective, the surface  
576 flux partitions towards higher latent heat flux under wet conditions (blue shadings in Fig. 5b) and  
577 towards higher sensible heat flux under intermediate (transitional and some wet) conditions (red  
578 shadings in Fig. 5b). Under dry conditions, changes in the partition factor are small, as are changes  
579 in SH and LH, except at the high soil moisture percentiles associated with rainy conditions.

580 The behavior of the repartition term in the atmospheric perspective contrasts with its behavior  
581 in the surface perspective: the atmospheric partition factor changes towards moistening under *all*  
582 conditions, although the magnitude of the repartition towards moisture is smallest in dry conditions  
583 in correspondence with the surface flux perspective (Fig. 5e). The inconsistency of the pattern in  
584 Fig. 5e compared to that in Fig. 5b reflects that, the atmosphere is responding to changes in land  
585 surface ET, but is generally getting moister under the influence of ocean as the globe warms. There  
586 is also a possible contribution from changes in the evaporation of precipitation, since it is a source  
587 of boundary layer specific humidity.

588 Having established the spatiotemporal structure of the key terms in our diagnostic equations, we  
589 test their relationship to the warming magnitude. Fig. 5c and f shows the warming magnitude in  
590 each of the  $50 \times 50$  bins as a function of the base-climate sensitivity, with the small dots color  
591 coded by the repartition term. This clearly demonstrates the relationship between the warming  
592 magnitude and the base-climate sensitivity in both perspectives: higher base-climate sensitivity  
593 (drier base-climate conditions) leads to a larger magnitude of warming. The larger dots show  
594 the temporally-averaged values of warming and base-climate sensitivity across the 50 AI bins,  
595 color-coded by the percentile of AI in each spatial bin. Here, we also see that climatologically arid  
596 regions warm the most and climatologically moist regions warm the least.

597 Eq. 6 and Eq. 7 suggest that if  $\Delta R_n$  and  $\Delta \text{MSE}$  are relatively uniform, and the repartition term  
598 is close to zero, the warming magnitude will scale linearly with the base-climate sensitivity. In  
599 Fig. 5c and f, we indeed see the general linear increase of  $\Delta T$  with  $1/\Psi$  and  $1/\psi$ . However,  
600 during the intermediate conditions between the very wet and dry (those with a surface sensitivity  
601 of  $0.2 \leq 1/\Psi \leq 0.8$ , and an atmospheric sensitivity of  $0.88 \leq 1/\psi \leq 0.93$ ), there is a spread in  $\Delta T$  at  
602 a given base climate sensitivity. This spread is consistent with the repartition terms (color shading  
603 of the dots). In these intermediate conditions, when surface flux partitions towards SH (red dots  
604 in Fig. 5c), the warming magnitude is amplified. Conversely, when surface flux partitions towards  
605 the LH (blue dots in Fig. 5c), the warming magnitude is dampened.

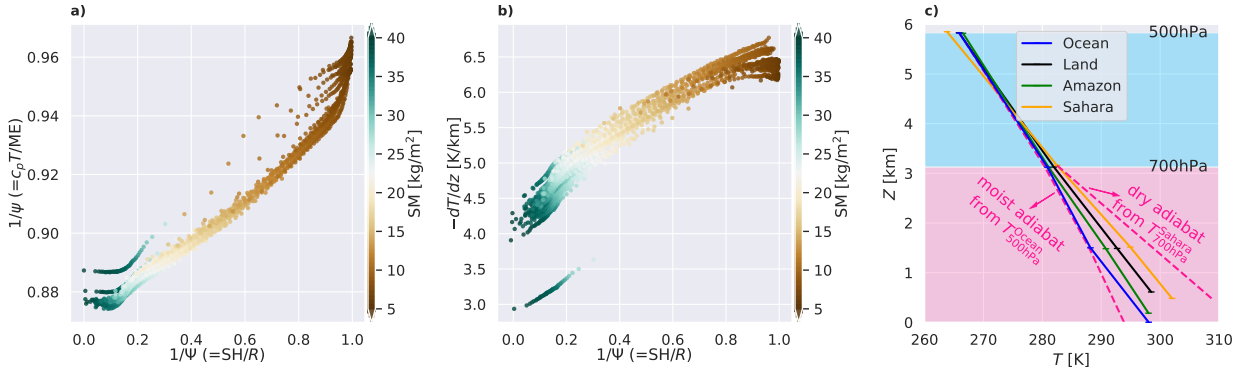
606 The similar and quasi-linear relationship (especially for the time-mean; the large dots in Fig. 5cf)  
607 between the warming magnitude and the base-climate sensitivity in both perspectives indicates  
608 that in climate models, the climatological dryness, both for the surface and the atmosphere, largely  
609 explains the spatial pattern of the warming magnitude. This is to say, we do not need drying of soil  
610 to explain the approximate spatial distribution of the *mean* warming. However, drying of soil and  
611 changes in the surface flux partition is important to explain the variability of warming at shorter  
612 time scales, especially during intermediate conditions between wet and dry.

## 613 **5. Discussion: the lower tropospheric temperature lapse rate and the surface fluxes**

614 The atmospheric perspective is top-down: starting from the same temperature in the free tropo-  
615 sphere constrained by WTG and moving downward, a larger mean lapse rate has to be associated  
616 with a higher surface air temperature, as well as a larger magnitude of surface air warming for a

617 given change in free tropospheric temperatures. Fig. 6c shows the temperature profiles over a few  
618 regions of different surface aridity in CMIP6 models for the base climate. They are, from moist  
619 to arid: the ocean averaged over the tropics (blue), the Amazon forest (green), the land averaged  
620 over the tropics (black), and the Sahara desert (orange). In the free troposphere (above roughly  
621 3 km), the temperature over the different regions is relatively uniform, and approximately follows  
622 the moist adiabat (the dashed pink line), as assumed in both Joshi et al. (2013) and the QE–WTG  
623 framework. In the lower troposphere, the temperature lapse is indeed closer to a dry adiabat for  
624 more arid regions, and closer to a moist adiabat for more moist regions, although in all cases  
625 the simulated lapse rate falls between these two edge cases. Note that the QE–WTG schematic  
626 (Fig. 1b; Byrne and O’Gorman 2013) is comparable to the lapse rate schematic (Fig. 1a; Joshi et al.  
627 2013) and the CMIP6-based lapse rates (Fig. 6c) because the higher the cloud base, the longer path  
628 in the lower troposphere where temperature follows the dry adiabat, the larger the mean lapse rate  
629 in the lower troposphere. In this context, the lower tropospheric lapse rate, the cloud base height,  
630 and the boundary layer RH are closely related, and variously act as the key control for the warming  
631 magnitude in the atmospheric perspective.

632 The surface perspective is bottom-up: temperature increases more when SH is higher for a given  
633 change in  $R_n$ . Fig. 6b shows a strong positive relationship between the mean temperature lapse  
634 rate in the lower troposphere and the ratio of SH to total turbulent flux  $R$  ( $SH/R$ , our base-climate  
635 sensitivity), where  $R = R_n - G = SH + LH \approx R_n$ . The outliers in the figure are the 50 temporal bins  
636 in the first AI bin, which are located at the edge of the Tibetan Plateau around Nepal. As mentioned  
637 in the context of Fig. 4a, this region has a very small AI due to a large amount of orographic  
638 precipitation, but the high orographic altitude makes the temperature lapse rate between 700 hPa  
639 and the surface small, since the level of 700 hPa is within the boundary layer. We can qualitatively  
640 understand the connection between the lapse rate and  $SH/R$  as follows: in drier regions, SH is a  
641 higher fraction of  $R$ , so the energy received by the surface is turbulently diffused into the boundary  
642 layer rather than (potentially) transported out as water vapor. In addition, drier regions also have  
643 less horizontal moisture convergence in the lower troposphere, which is associated with less rain.  
644 Higher SH and lack of rain at the surface result in a warmer surface air relative to aloft; combined  
645 with WTG in the free troposphere, the warmer surface air over drier regions yields a larger mean  
646 temperature lapse rate in the lower troposphere.



647 FIG. 6. The relationship between the base-climate (a) atmospheric sensitivity  $1/\psi$  and surface sensitivity  $1/\Psi$ ,  
 648 (b) temperature lapse rate between the 700 hPa level and the near surface level ( $-dT/dz$ ) and surface sensitivity  
 649  $1/\Psi$  (the fraction of SH in the total enthalpy flux  $R$ ), and (c) warm season mean temperature profiles during  
 650 1850–1879 from CMIP6 models (see Section 2 for details), averaged over tropical (30S–30N) ocean (blue),  
 651 tropical land (black), Amazon forest (15°S–0°, 70°W–55°W; green) and Sahara desert (20°N–30°N, 10°E–30°E,  
 652 orange). The two pink dashed lines in panel c illustrate the temperature profile below 700 hPa if following the  
 653 dry adiabat (right side, starting with temperature at 700 hPa over the Sahara desert and integrating downward),  
 654 and the temperature profile below 500 hPa if following the moist adiabat (left side, starting with temperature at  
 655 500 hPa averaged over the tropical ocean and integrating downward).

## 656 6. Summary and outlook

657 Motivated to better understand the amplified warming over tropical land and its association with  
 658 dry conditions, we compare the two existing perspectives in the field that aim to explain the “drier–  
 659 warmer” phenomenon. One is based on the atmospheric dynamics of the tropical troposphere (the  
 660 atmospheric dynamics perspective), and the other focuses on land surface processes (the surface  
 661 flux perspective). The atmospheric dynamics perspective uses moist static energy as a constrained  
 662 quantity, and derives the amplified warming from lower (base-climate) specific humidity. The  
 663 surface flux perspective uses the net radiation at the surface as a constrained total, and centers its  
 664 argument on reduced water availability due to soil drying and/or plant-moderated reductions in  
 665 transpiration, which results in a change in the partitioning between the sensible and the latent heat  
 666 fluxes.

667 Based on climate model outputs, we first present a comparison of the full spatiotemporal distri-  
 668 bution of the relevant variables in the two perspectives in the AI/SM phase space (Fig. 2 and 3) and

669 discuss the applicability of the equal MSE assumption in the QE-WTG framework in explaining the  
670 spatiotemporal variability. By comparing the full spatiotemporal distribution, we address the first  
671 question we raise in the beginning on how key variables in the two perspectives correspond to each  
672 other. We also examine the connection of the moisture constraint in the atmospheric perspective  
673 to surface conditions, where we show how the neglect of changes in local evapotranspiration in  
674 the atmospheric perspective and the neglect of atmospheric processes in the surface perspective  
675 may lead to deviations (Fig. 4). From here, we can better understand the second question we  
676 raise, how the dryness measures between the two perspectives relate to each other. We then use a  
677 diagnostic linearized perturbation framework to relate the temperature response to a base-climate  
678 sensitivity, changes in the MSE or  $R_n$ , and changes in the warming versus moistening partition  
679 factor. We show that the base climate sensitivity largely explains the warming magnitude across  
680 spatiotemporal conditions: drier base-climate conditions have a larger base-climate sensitivity and  
681 experience a larger magnitude of warming. This relationship between the warming magnitude  
682 and the base-climate sensitivity holds particularly well for the time mean, and the surface and the  
683 atmospheric perspectives correspond well in terms of this role of the base-climate sensitivity. On  
684 top of the quasi-linear relationship between the warming magnitude and the base-climate sensitiv-  
685 ity, changes in the partition factor between warming and moistening for intermediate (between wet  
686 and dry) conditions further enhance or dampen the warming magnitude (Fig. 5). This informs us  
687 on the third question we raise, how climatological dryness versus changes in dryness contribute to  
688 amplified warming in each perspective. Lastly, through linking the lower tropospheric lapse rate  
689 with the surface fluxes (Fig. 6), we provide mechanistic insights on how the top-down atmospheric  
690 perspective connects with the bottom-up surface perspective. The comparison of the two perspec-  
691 tives in our study reveals how key arguments of the two perspectives hold across the spatiotemporal  
692 conditions and advances our understanding of the drier-warmer relationship. Our analyses are  
693 based on CMIP6 model output and are largely diagnostic; comparisons with observations and  
694 further quantifying the contribution from specific land surface and atmospheric processes can be  
695 informative.

696 *Acknowledgments.* The authors acknowledge the support from the NSF grant 1939988. We  
697 thank three anonymous reviewers for helpful reviews and the editor for handling the manuscript.  
698 S.Q.D. appreciates helpful conversations with Dr. Zhihong Tan and Dr. Mengxi Wu. The authors  
699 also acknowledge the World Climate Research Programme, which, through its Working Group on  
700 Coupled Modelling, coordinated and promoted CMIP6. We thank the climate modeling groups for  
701 producing and making available their model output, the Earth System Grid Federation (ESGF) for  
702 archiving the data and providing access, and the multiple funding agencies who support CMIP6 and  
703 ESGF. I.R.S. acknowledges funding from the National Center for Atmospheric Research, which is  
704 a major facility sponsored by the National Science Foundation under the Cooperative Agreement  
705 1852977.

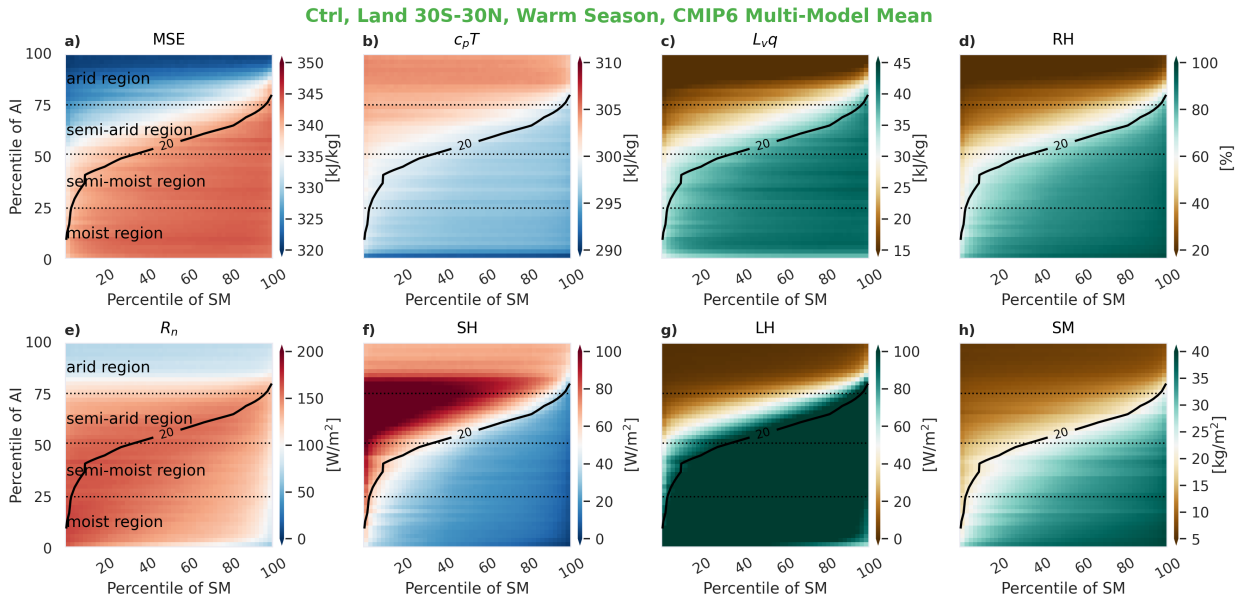
706 *Data availability statement.* CMIP6 model outputs used in this study can be downloaded from  
707 the CMIP6 data archive (<https://esgf-node.llnl.gov/search/cmip6/>). ERA5 reanalysis data can be  
708 downloaded from the ECMWF Climate Data Store (<https://cds.climate.copernicus.eu/>). Jupyter  
709 Notebooks for analyzing the data will be shared through GitHub at the acceptance of this paper.

710

## APPENDIX A

711

### **Spatiotemporal distribution of relevant variables in the base climate state**



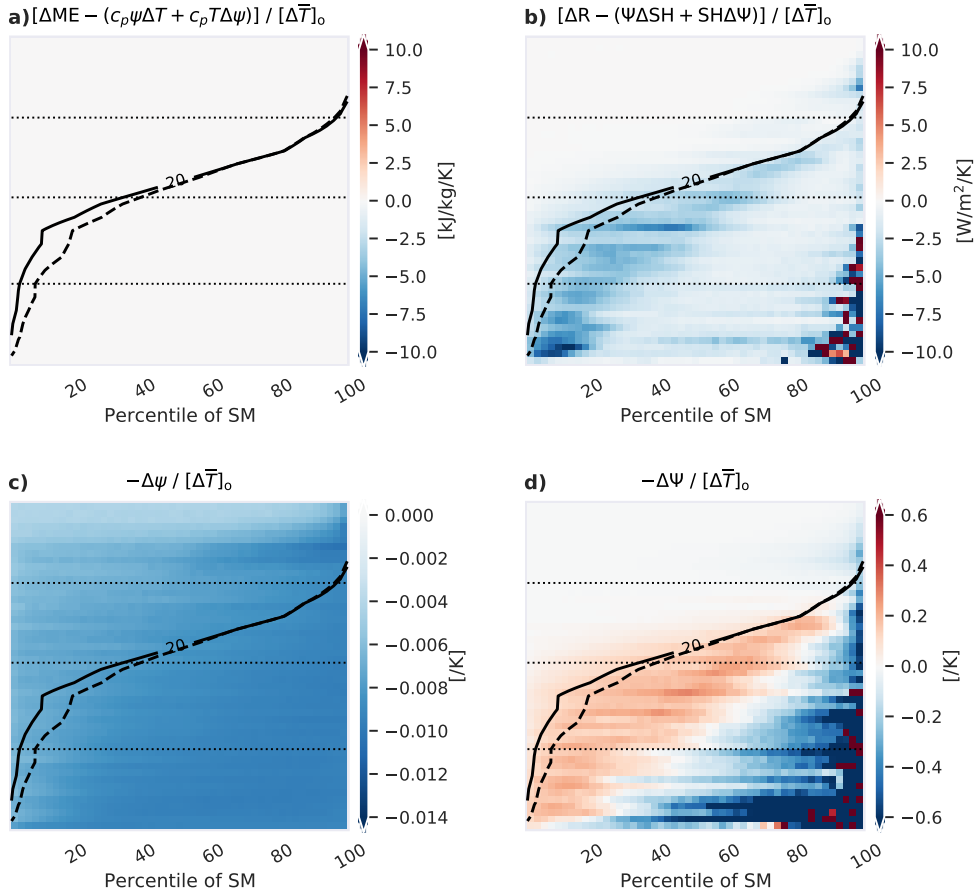
712 FIG. A1. The spatiotemporal distribution of the base-climate surface air (a) moist static energy (MSE), (b)  
 713 temperature converted to energy units ( $c_p T$ ), (c) specific humidity converted to energy units ( $L_v q$ ), (d) relative  
 714 humidity (RH), and the surface (e) net radiation ( $R_n$ ), (f) sensible heat flux (SH), (g) latent heat flux (LH), (h)  
 715 soil moisture (SM) in the phase space of daily soil moisture percentile and climatological aridity index (AI)  
 716 percentile. The black contour shows the critical SM of  $20 \text{ kg m}^{-2}$ .

717

## APPENDIX B

718

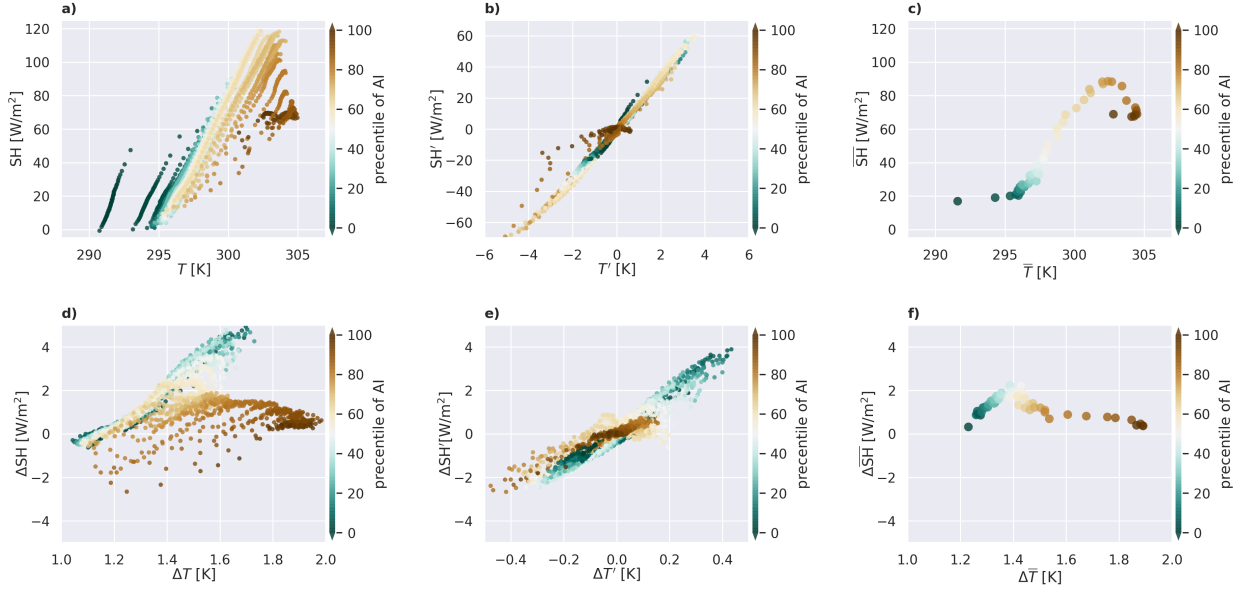
### Additional information for terms in the diagnostic perturbation equations



719 FIG. B1. (a) The residuals from the linearization in Eq. 3; (b) the residuals from the linearization in Eq. 4;  
 720 (c) changes in the atmospheric partition factor  $-\Delta\psi$ ; (d) changes in the surface partition factor  $-\Delta\Psi$ . The fact  
 721 that the patterns in (c) and (d) are similar to patterns in Fig. 5be indicates that the spatiotemporal distribution  
 722 of changes in the partition factor ( $-\Delta\psi$  and  $-\Delta\Psi$ ) dominates the spatiotemporal distribution of the repartition  
 723 terms ( $-c_p T \Delta\psi$  and  $-SH \Delta\Psi$ ).

## 724 APPENDIX C

### 725 The relationship between perturbations in the surface sensible heat flux and perturbations 726 in temperature



727 FIG. C1. The relationship between (a) the base-climate surface sensible heat flux (SH) and surface air  
 728 temperature ( $T$ ); (b) the base-climate temporal anomalies in SH and  $T$ , with the local temporal-mean value  
 729 removed, (c) the local temporal-mean SH and  $T$ ; (d) the climate changes in SH and  $T$ ; (e) the temporal anomalies  
 730 of changes in SH and  $T$  with the local temporal-mean change removed; (f) the local temporal-mean changes in  
 731 SH and  $T$ . All scatters are color-coded by the percentile of the aridity index (AI). In panels a, b, d, and e, each  
 732 scatter represents one of the  $50 \times 50$  spatio-temporal bins, and in panels c and f, each scatter represents one of  
 733 the 50 spatial bin, with the temporal dimension averaged out.

734 In the perturbation relation we use for the surface energy balance (Eq. 5), we have linearized  
 735 the perturbation in the surface sensible heat flux (SH) as a coefficient  $\kappa$  times the temperature  
 736 perturbation. Fig. C1 examines to what extent this linearization is justifiable.

737 The first row shows the relationships between SH and  $T$  in the base climate. Panel b informs  
 738 us that temporal perturbations in SH and  $T$  relate to each other linearly by a similar coefficient  
 739 (approximately  $15\text{--}20 \text{ W/m}^2/\text{K}$ ) across locations, except in the very dry locations. Panel c informs  
 740 us that spatial anomalies of the mean SH and  $T$  also relates to each other linearly except the very  
 741 moist and very dry locations.

742 The second row shows the relationships between changes in SH and  $T$  under climate change.  
 743 For our particular application of the linearized perturbation relation Eq. 5, panel (d) is the most  
 744 relevant. It shows us that for moist and semi-moist conditions,  $\Delta SH$  and  $\Delta T$  have relatively good

745 linear relationship, while the relationship for dry regions is weaker. If we remove the mean at each  
746 location and only focus on the temporal anomalies, then all locations show a linear relationship  
747 (panel e), with the regression coefficient, i.e.,  $\kappa$ , being approximately  $5 \text{ W/m}^2/\text{K}$  for dry locations  
748 and  $10 \text{ W/m}^2/\text{K}$  for moist locations. There is no linear relationship between the time-mean change  
749 in SH and  $T$  across locations (panel f).

750 Since in our analysis, the data we use retains the temporal variability and we emphasize the  
751 qualitative understanding, we accept simply linearizing  $\Delta\text{SH}$  as  $\kappa\Delta T$ . With this linearization we  
752 can derive Eq. 7, and we have the surface sensitivity as  $1/(\kappa\Psi)$ . We assume  $\kappa$  is the same constant  
753 across spatiotemporal conditions and focus on the sensitivity factor  $1/\Psi$ . The non-uniformity of  $\kappa$   
754 will make quantitative predictions of the warming magnitude more complicated; although here we  
755 see that it may be approached by separating dry and moist conditions.

## 756 **References**

- 757 Arakawa, A., and W. H. Schubert, 1974: Interaction of a cumulus cloud ensemble with the  
758 large-scale environment, Part I. *Journal of the atmospheric sciences*, **31 (3)**, 674–701.
- 759 Berg, A., B. R. Lintner, K. L. Findell, S. Malyshev, P. C. Loikith, and P. Gentine, 2014: Impact of  
760 soil moisture–atmosphere interactions on surface temperature distribution. *Journal of Climate*,  
761 **27 (21)**, 7976–7993.
- 762 Betts, A. K., 2009: Land-surface-atmosphere coupling in observations and models. *Journal of*  
763 *Advances in Modeling Earth Systems*, **1 (3)**.
- 764 Byrne, M. P., 2021: Amplified warming of extreme temperatures over tropical land. *Nature*  
765 *Geoscience*, **14 (11)**, 837–841.
- 766 Byrne, M. P., and P. A. O’Gorman, 2013: Land–ocean warming contrast over a wide range of  
767 climates: Convective quasi-equilibrium theory and idealized simulations. *Journal of Climate*,  
768 **26 (12)**, 4000–4016.
- 769 Byrne, M. P., and P. A. O’Gorman, 2016: Understanding decreases in land relative humidity  
770 with global warming: Conceptual model and GCM simulations. *Journal of Climate*, **29 (24)**,  
771 9045–9061.
- 772 Byrne, M. P., and P. A. O’Gorman, 2018: Trends in continental temperature and humidity directly  
773 linked to ocean warming. *Proceedings of the National Academy of Sciences*, 201722312.
- 774 Chadwick, R., P. Good, and K. Willett, 2016: A simple moisture advection model of specific  
775 humidity change over land in response to SST warming. *Journal of Climate*, **29 (21)**, 7613–  
776 7632.
- 777 Chan, D., A. Rigden, J. Proctor, P. W. Chan, and P. Huybers, 2022: Differences in radiative forcing,  
778 not sensitivity, explain differences in summertime land temperature variance change between  
779 CMIP5 and CMIP6. *Earth’s Future*, **10 (2)**, e2021EF002402.
- 780 Dirmeyer, P. A., G. Balsamo, E. M. Blyth, R. Morrison, and H. M. Cooper, 2021: Land-atmosphere  
781 interactions exacerbated the drought and heatwave over northern Europe during summer 2018.  
782 *AGU Advances*, **2 (2)**, e2020AV000283.

783 Donat, M. G., A. J. Pitman, and S. I. Seneviratne, 2017: Regional warming of hot extremes  
784 accelerated by surface energy fluxes. *Geophysical Research Letters*, **44** (13), 7011–7019.

785 Duan, S. Q., K. L. Findell, and S. A. Fueglistaler, 2023: Coherent mechanistic patterns of tropical  
786 land hydroclimate changes. *Geophysical Research Letters*, **50** (7), e2022GL102285.

787 Duan, S. Q., K. L. Findell, and J. S. Wright, 2020: Three regimes of temperature distribution change  
788 over dry land, moist land and oceanic surfaces. *Geophysical Research Letters*, e2020GL090997,  
789 <https://doi.org/https://doi.org/10.1029/2020GL090997>.

790 Emanuel, K. A., J. David Neelin, and C. S. Bretherton, 1994: On large-scale circulations in  
791 convecting atmospheres. *Quarterly Journal of the Royal Meteorological Society*, **120** (519),  
792 1111–1143.

793 Eyring, V., S. Bony, G. A. Meehl, C. A. Senior, B. Stevens, R. J. Stouffer, and K. E. Taylor, 2016:  
794 Overview of the Coupled Model Intercomparison Project Phase 6 (CMIP6) experimental design  
795 and organization. *Geoscientific Model Development*, **9** (5), 1937–1958.

796 Fu, Q., and S. Feng, 2014: Responses of terrestrial aridity to global warming. *Journal of Geophys-*  
797 *ical Research: Atmospheres*, **119** (13), 7863–7875.

798 Held, I. M., and K. M. Shell, 2012: Using relative humidity as a state variable in climate feedback  
799 analysis. *Journal of Climate*, **25** (8), 2578–2582.

800 Joshi, M., F. Lambert, and M. Webb, 2013: An explanation for the difference between twentieth  
801 and twenty-first century land–sea warming ratio in climate models. *Climate Dynamics*, **41** (7),  
802 1853–1869.

803 Joshi, M. M., J. M. Gregory, M. J. Webb, D. M. Sexton, and T. C. Johns, 2008: Mechanisms for  
804 the land/sea warming contrast exhibited by simulations of climate change. *Climate Dynamics*,  
805 **30** (5), 455–465, <https://doi.org/https://doi.org/10.1007/s00382-007-0306-1>.

806 Kong, W., K. A. McKinnon, I. R. Simpson, and M. M. Laguë, 2023: Understanding responses of  
807 summer continental daily temperature variance to perturbations in the land surface evaporative  
808 resistance. *Journal of Climate*, **36** (6), 1653–1678.

- 809 Koster, R. D., and S. P. Mahanama, 2012: Land surface controls on hydroclimatic means and  
810 variability. *Journal of Hydrometeorology*, **13** (5), 1604–1620.
- 811 McColl, K. A., and A. J. Rigden, 2020: Emergent simplicity of continental evapotranspiration.  
812 *Geophysical Research Letters*, **47** (6), e2020GL087101.
- 813 McColl, K. A., G. D. Salvucci, and P. Gentine, 2019: Surface flux equilibrium theory explains an  
814 empirical estimate of water-limited daily evapotranspiration. *Journal of Advances in Modeling  
815 Earth Systems*, **11** (7), 2036–2049.
- 816 Milly, P. C., and K. A. Dunne, 2016: Potential evapotranspiration and continental drying. *Nature  
817 Climate Change*, **6** (10), 946–949.
- 818 Neelin, J. D., and N. Zeng, 2000: A quasi-equilibrium tropical circulation model–formulation.  
819 *Journal of the atmospheric sciences*, **57** (11), 1741–1766.
- 820 Roe, G., 2009: Feedbacks, timescales, and seeing red. *Annual Review of Earth and Planetary  
821 Sciences*, **37** (1), 93–115.
- 822 Seneviratne, S. I., T. Corti, E. L. Davin, M. Hirschi, E. B. Jaeger, I. Lehner, B. Orlowsky, and A. J.  
823 Teuling, 2010: Investigating soil moisture–climate interactions in a changing climate: A review.  
824 *Earth-Science Reviews*, **99** (3-4), 125–161.
- 825 Sherwood, S., and Q. Fu, 2014: A drier future? *Science*, **343** (6172), 737–739.
- 826 Sobel, A. H., and C. S. Bretherton, 2000: Modeling tropical precipitation in a single column.  
827 *Journal of climate*, **13** (24), 4378–4392.
- 828 Sutton, R. T., B. Dong, and J. M. Gregory, 2007: Land/sea warming ratio in response to climate  
829 change: IPCC AR4 model results and comparison with observations. *Geophysical research  
830 letters*, **34** (2).
- 831 Van der Ent, R. J., H. H. Savenije, B. Schaefli, and S. C. Steele-Dunne, 2010: Origin and fate of  
832 atmospheric moisture over continents. *Water Resources Research*, **46** (9).
- 833 Vargas Zeppetello, L., and D. Battisti, 2020: Projected increases in monthly midlatitude summer-  
834 time temperature variance over land are driven by local thermodynamics. *Geophysical Research  
835 Letters*, **47** (19), e2020GL090197.

- 836 Vogel, M. M., R. Orth, F. Cheruy, S. Hagemann, R. Lorenz, B. Hurk, and S. I. Seneviratne, 2017:  
837 Regional amplification of projected changes in extreme temperatures strongly controlled by soil  
838 moisture-temperature feedbacks. *Geophysical Research Letters*, **44** (3), 1511–1519.
- 839 Zelinka, M. D., T. A. Myers, D. T. McCoy, S. Po-Chedley, P. M. Caldwell, P. Ceppi, S. A. Klein,  
840 and K. E. Taylor, 2020: Causes of higher climate sensitivity in CMIP6 models. *Geophysical*  
841 *Research Letters*, **47** (1), e2019GL085 782.
- 842 Zeppetello, L. V., É. Tétréault-Pinard, D. Battisti, and M. Baker, 2020: Identifying the sources  
843 of continental summertime temperature variance using a diagnostic model of land–atmosphere  
844 interactions. *Journal of Climate*, **33** (9), 3547–3564.
- 845 Zhang, Y., and S. Fueglistaler, 2020: How tropical convection couples high moist static energy  
846 over land and ocean. *Geophysical Research Letters*, **47** (2), e2019GL086 387.